Supplement of The Cryosphere, 16, 277–295, 2022
https://doi.org/10.5194/tc-16-277-2022-supplement

The Cryosphere
Open Access

Supplement of

Ice-shelf ocean boundary layer dynamics from large-eddy simulations

Carolyn Branecky Begeman et al.

Correspondence to: Carolyn Branecky Begeman (cbegeman@lanl.gov)

Contents of this file

Table 1. Parameters relevant to the configuration of referenced simulations. Asterisks denote variables whose values were varied between simulations.

Variable	Description	Value
c_d	drag coefficient	0.003
c_p	heat capacity of water	4218
$dP/dx, dP/dy$	horizontal pressure gradient	$0.0, 0.03$ Pa m^{-1}
dS/dz	far-field vertical salinity gradient	0.5 PSU km^{-1}
$d\theta/dz$	far-field vertical temperature gradient	0.1 °C km^{-1}
h_x, h_y	domain width	64 m
h_z	domain height	64 m
L_f	latent heat of fusion	3.3×10^5 J kg^{-1}
P_0	domain top pressure	800 dbar
Pr	Prandtl number	13.8
rdf	Rayleigh damping coefficient	0.0001
S_∞	far-field salinity	35 PSU
Sc	Schmidt number	2432
α	*ice shelf slope	0.01 to 1.0°
β	angle between vector oriented up-slope and North	90°
β_m	Businger coefficient for momentum	-4.8
β_θ	Businger coefficient for temperature	-5.6
β_S	Businger coefficient for salinity	-5.6
Δ_x, Δ_y	horizontal resolution	0.5 m
Δ_z	vertical resolution	0.25 m
$\Gamma_{\theta,mol}$	thermal molecular exchange coefficient	$12.5\mathrm{Pr}^{2/3} - 6$
$\Gamma_{S,mol}$	salt molecular exchange coefficient	$12.5\mathrm{Sc}^{2/3} - 6$
Γ_f	destabilizing transfer coefficient	5.7×10^{-3}
ϕ	latitude	-70°S
θ_∞	*far-field temperature	-2.4 to -1.9°C

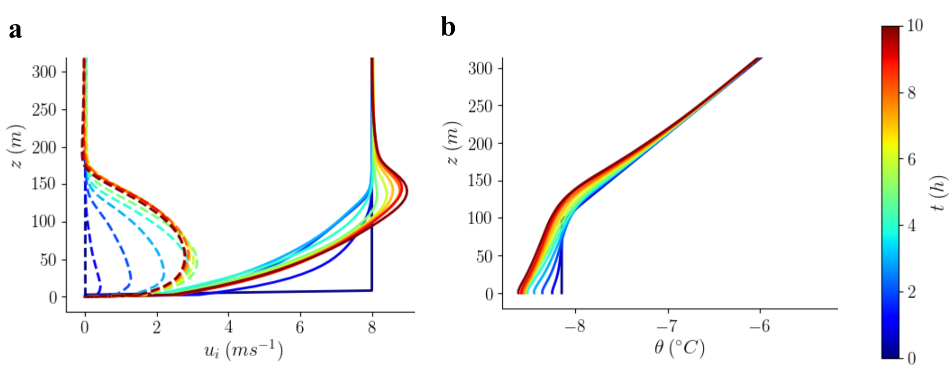

Figure S1. Results of the atmospheric stable boundary layer test case presented in Abkar and Moin (2017) using PALM with the Anisotropic Minimum Dissipation (AMD) turbulence closure. Compare with their Figure 1.

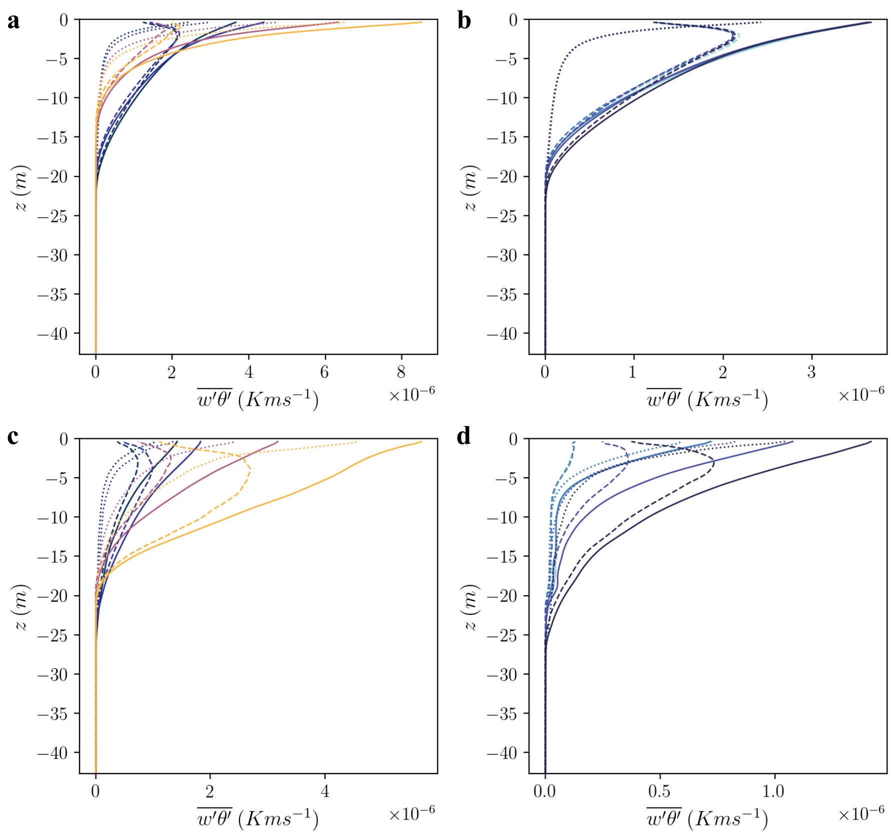

Figure S2. Vertical heat flux depth-profiles averaged over one inertial period for (a,c) thermal driving simulations and (b,d) variable slope simulations. Profiles shown in (a,b) are averaged over the first inertial period after a 2 h spin-up, (b,d) over the last inertial period. Solid lines represent the total flux, dashed resolved flux and dotted subgrid flux. Colors correspond to those shown in Figure 1.

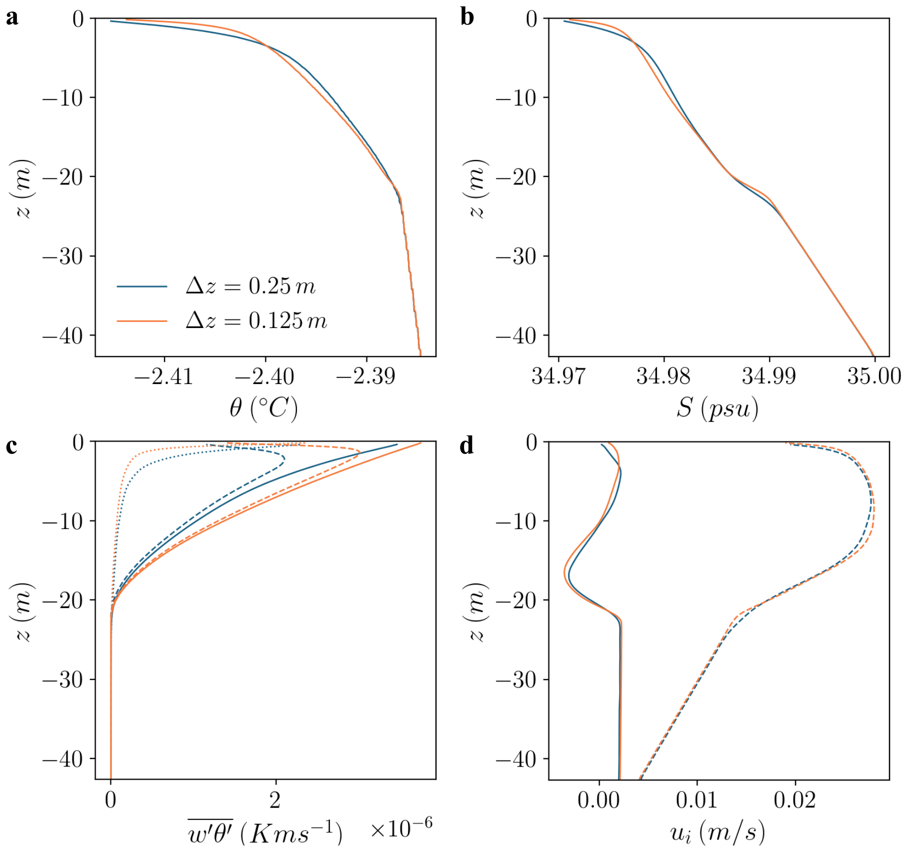

Figure S3. Sensitivity of simulated mean state and turbulent fluxes to resolution. The vertical resolution is double the horizontal resolution ($\Delta x, \Delta y$). Results are averaged over the first inertial period after a 2h spin-up. (a) Temperature. (b) Salinity. (c) Total vertical heat flux (solid), resolved vertical heat flux (dashed), and sub-grid vertical heat flux (dotted). (d) Velocity, u-component (solid) and v-component (dashed).

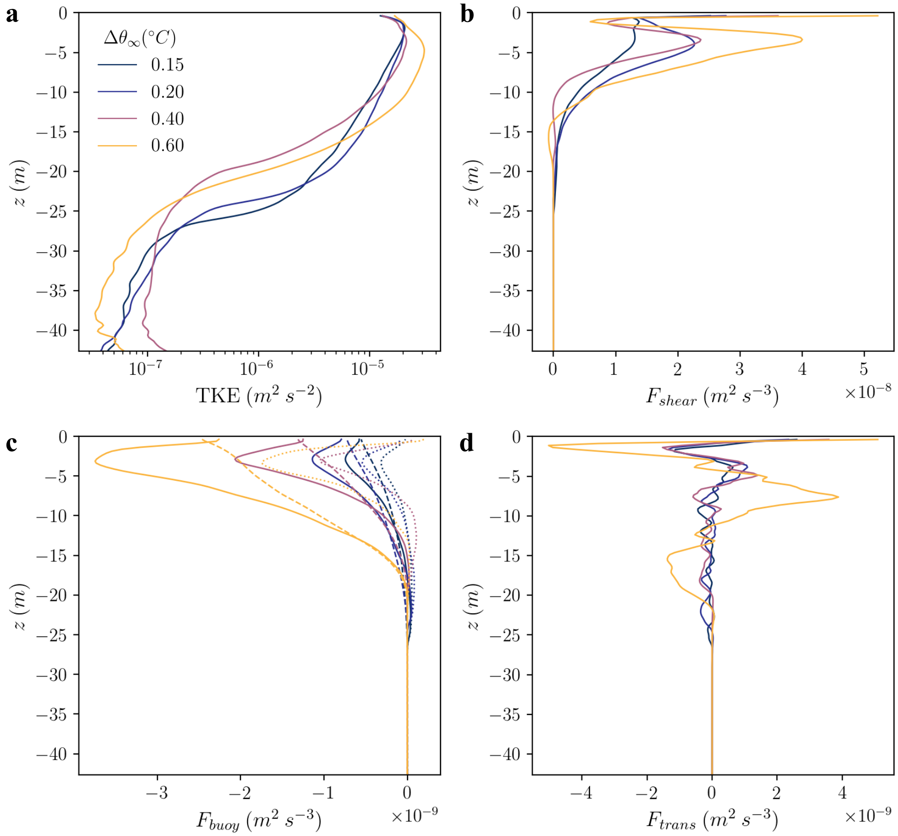

Figure S4. (a) Simulated turbulent kinetic energy for variable thermal driving simulations averaged over the last inertial period and (b-d) turbulent kinetic energy production terms over the same period. (b) Shear production. (c) Buoyancy production. The total buoyancy production is shown with solid lines, vertical component dashed, and upslope component dotted. (d) TKE transport. Positive denotes production, negative destruction. Note that the x-axis scales differ between panels.

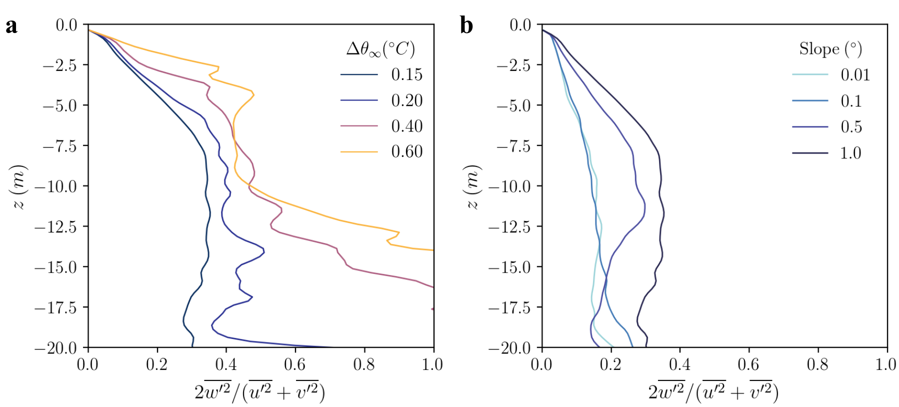

Figure S5. Ratio of vertical to horizontal velocity variance for (a) thermal driving simulations and (b) variable slope simulations averaged over the last inertial period.

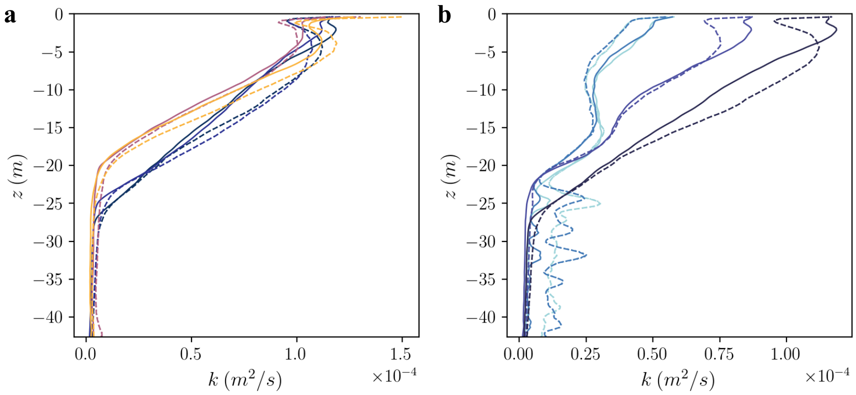

Figure S6. Sub-grid vertical diffusivities for momentum (solid), heat (dashed) and salt (dotted) for (a) thermal driving simulations and (b) variable slope simulations. Heat and salt diffusivities curves are visually indistinguishable.

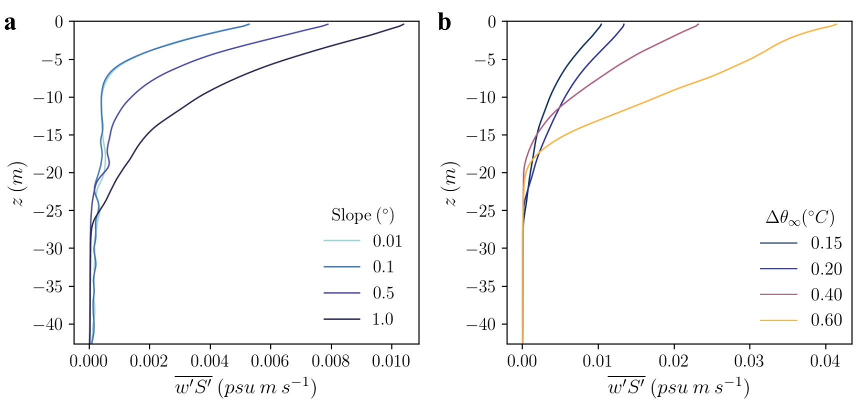

Figure S7. Total vertical salt flux depth-profiles averaged over one inertial period for (a) thermal driving simulations and (b) variable slope simulations.

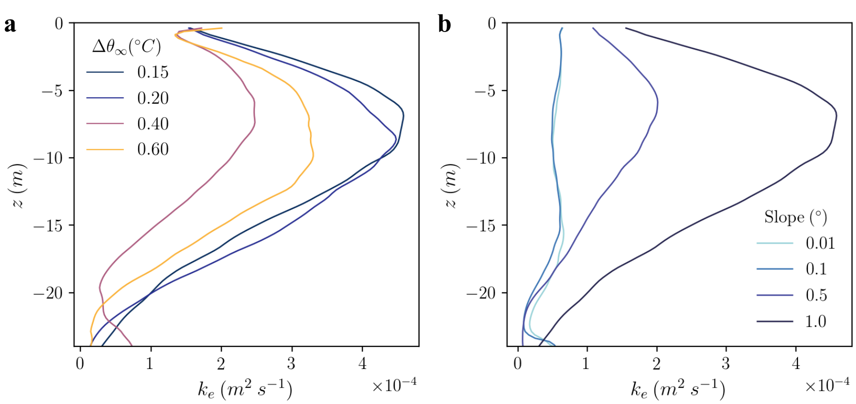

Figure S8. Vertical eddy viscosity from (a) thermal driving simulations and (b) slope-varying simulations over the last inertial period. Depths below -20 m are not shown as the eddy viscosity is only used to compute the Ekman depth within the IOBL.

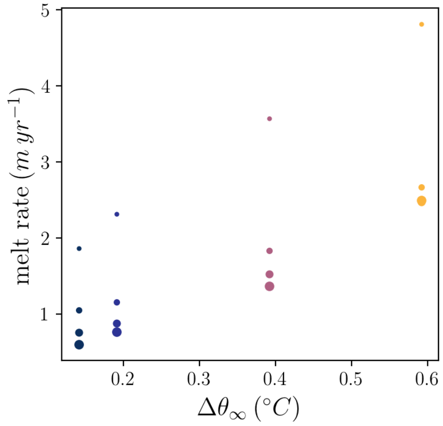

Figure S9. Relationship between far-field thermal driving and melt rate. This figure is the same as Figure 7a but values are averaged over each inertial cycle. The largest points correspond to the fourth and last inertial cycle with progressively smaller points for previous inertial cycles.